

## **Coastal Engineering Journal**



ISSN: 2166-4250 (Print) 1793-6292 (Online) Journal homepage: https://www.tandfonline.com/loi/tcej20

# Solitary wave impacts on vertical and overhanging near-coast structures

Mei Huang, Andrew Kennedy, Tori Tomiczek & Joannes Westerink

To cite this article: Mei Huang, Andrew Kennedy, Tori Tomiczek & Joannes Westerink (2018) Solitary wave impacts on vertical and overhanging near-coast structures, Coastal Engineering Journal, 60:3, 356-370, DOI: 10.1080/21664250.2018.1542963

To link to this article: <a href="https://doi.org/10.1080/21664250.2018.1542963">https://doi.org/10.1080/21664250.2018.1542963</a>

	Published online: 11 Nov 2018.
	Submit your article to this journal 🗷
ılıl	Article views: 45
CrossMark	View Crossmark data 🗗





## Check for updates

#### ORIGINAL RESEARCH PAPER

## Solitary wave impacts on vertical and overhanging near-coast structures

Mei Huang<sup>a</sup>, Andrew Kennedy<sup>b</sup>, Tori Tomiczek<sup>c</sup> and Joannes Westerink<sup>b</sup>

<sup>a</sup>Department of Aerospace and Mechanical Engineering, University of Notre Dame, Notre Dame, USA; <sup>b</sup>Department of Civil and Environmental Engineering and Earth Sciences, University of Notre Dame, Notre Dame, USA; <sup>c</sup>Department of Naval Architecture and Ocean Engineering, United States Naval Academy, Annapolis, USA

#### **ABSTRACT**

In this paper, we investigate short-duration solitary wave impacts on overhanging near-coast structures, which are represented here as rectangular blocks protruding out from a vertical wall. Wave transformation is computed for a variety of scenarios using the OpenFOAM variant IHFOAM. In agreement with previous studies, the largest pressures and loads occur when there is a violent impact with near-breaking or just-broken waves on the wall, causing a strong vertical jet. This condition most easily occurs with steep near-shore slopes. Maximum vertical loads on overhangs occur at significantly higher block elevations than are found for maximum horizontal loads. Overhang lengths have small effects on magnitudes of horizontal forces, but strongly increase positive uplift vertical loads. Although maximum instantaneous vertical loads can significantly exceed instantaneous horizontal loads, time-averaged vertical loads decrease rapidly with increasing averaging period while horizontal loads show more modest decreases; horizontal loads significantly exceed vertical loads for large averaging periods. This indicates that the pressure-impulse in the wall-generated vertical jets is much less than that arising from the horizontal solitary wave impacts.

#### **ARTICLE HISTORY**

Received 28 November 2017 Accepted 18 October 2018

#### **KEYWORDS**

Water wave; solitary wave; coastal structure; overhang; wave loading

#### 1. Introduction

Coastal regions form the core of the world's most densely populated lands (NOAA, 2013); however, the threat of natural disasters, such as tsunamis or typhoons, is always present. Taking one widely viewed example, a coastal residence during Super Typhoon Haiyan was inundated rapidly from dry land to complete destruction in less than 10 s (Gensis, 2013), with wave amplitudes of several meters and velocities exceeding 5 m/s generating loads sufficient to cause catastrophic damage. Similar levels of damage have been observed on many other occasions (Lay et al., 2005; Mori and Takahashi, 2012) arising from high velocity wave action on structures. However, although much work has been performed on the mechanisms and magnitudes of wave loading (Yim et al., 2014; Yan et al., 2015; Tomiczek et al., 2016), there still remain many fundamental situations that are not entirely understood.

This paper investigates how wave loads impact overhanging structures on top of vertical walls. Overhangs may be found on many near-coast structures ranging from seawalls (Kisacik, Troch, and Philippe, 2012) to buildings located on normally dry ground. Even though wave loads at vertical walls have long been studied, research on overhanging loading is limited. Wave loads on overhangs can also be significant in widely varied fields such as clifftop boulder transport (Cox et al., 2012; Kennedy et al., 2017),

where the motion of large rocks is often used to estimate storm or tsunami intensity in the absence of additional historical information.

Wave loads at walls represent a canonical scenario for structural design along coastlines that has long been studied using both experimental and numerical methods. Experimentally, Lugni, Brocchini, Faltinsen (2006) reported the pressure magnitude on a vertical wall under wave sloshing, while Cuomo et al. (2010) studied loading at a vertical wall under irregular breaking waves. Robertson et al. (2013) recorded the lateral forces on a vertical wall, and later Shafiei, Melville, and Shamseldin (2016) investigated pressures on an oriented square prism. Both of these studies considered the impact of a tsunami bore. Overall, laboratory results show that hydrodynamic forces are dominant over hydrostatic forces when waves impact vertical structures, arising from the large and rapid changes in fluid velocities as waves encounter the wall. Laboratory experiments have provided the great majority of data points in the field of wave loading; limitations of these studies include two-dimensionality in narrow wave flumes, and scale-effects of trapped air compressibility and bubble breakup in laboratory tanks when compared to field-scale waves.

The most comprehensive study, by far, of wave loads on walls was carried out by the European Union PROVERBS campaign (Oumeraci et al., 1999).

This multi-investigator project examined hydrodynamic, geotechnical, structural, and reliability aspects of wave loads for four main types of vertical breakwaters (none of which had the overhangs considered here). Consideration of hydrodynamics led to four main loading regimes: (a) standing waves; (b) slightly breaking waves; (c) broken waves; and (d) impact loads. Due to the time variations of the loading, different loading regimes required different structural approaches: for the first three types, "quasi-static" approaches were deemed suitable, while "dynamic analysis" was employed for impact loads as the time scales of loading overlapped the time scales of structural response. Detailed probabilistic loading and design standards were detailed using a very large number of experimental results from laboratory to field scale.

In addition to laboratory research, numerical and theoretical studies have been conducted by many scientists. Cooker, Weidman, and Bale (1997) investigated loading on a vertical wall using a perturbation method to find the maximum force from nonbreaking solitary waves as a function of the incident wave amplitude. Smoothed particle hydrodynamics (SPH) investigations by Altomare et al. (2015), Didier et al. (2014), and Germain et al. (2014) reached the same conclusion as found in the laboratory experiments, namely that hydrodynamic forces are dominant.

Traditional computational fluid dynamics (CFD) methods, including Reynolds-averaged Navier-Stokes equations (RANS) and large eddy simulation (LES), have also been applied to wave loading problems. Full LES is not commonly used in large scale wave problems because of its high computational costs; RANS simulations are more prevalent (Kleefsman et al., 2005), for example, the widely used interFoam solver from the open source software OpenFoam (Greenshields, 2015) computes two phase RANS equations for incompressible flow. The general reliability of interFoam was studied by Deshpande, Anumolu, and Trujillo (2012), who showed that it can capture unsteady flow physics with relatively modest grid resolutions. Paczkowski et al. (2014) studied wave loads on a vertical wall with this technique, validating their work by comparing numerical dam break loads with experimental data.

Most recently, a newly developed wave solver IHFOAM, an extension to the OpenFOAM model developed by IH Cantabria, Spain, is able to couple the interFoam solver with wave generation-absorption boundaries. Jacobsen, Fuhrman, and Fredse (2012) first extended interFoam with these new boundaries. Higuera, Lara, and Losada (2013a, 2013b) and Iturrioz et al. (2015) validated the IHFOAM solver, and showed a good agreement between IHFOAM simulations and experimental results in terms of pressure, velocity, and surface elevation. These studies have shown the IHFOAM solver to have good accuracy for situations like wave runup on structures.

All of these numerical studies have limiting assumptions—for two-phase air-water computations, the most common limitations are the two-dimensional approximations that are often used to reduce computational expense, the incompressible air assumption, and lack of sufficient resolution to resolve details of jets as waves impact a structure. For SPH methods, computations are often single-phase (water only), and have artificially compressible flow that can affect peak loading. Still, many of these limitations are only applicable when examining very short time scales, and do not affect momentum-impulse considerations that govern overall behavior on longer time scales.

This paper studies incompressible two-phase solitary wave loading on overhanging structures numerically using IHFOAM, with a  $k - \epsilon$  turbulence model. Large loading is expected when the wave breaks directly on the structure, and we will examine how these loads are influenced by the wave height, the shape of the bathymetry, and the size of the overhang. The paper is organized as follows: details of the numerical model, including validation examples, are provided in Section 2. Section 3 examines solitary wave loading on overhangs for a variety of incident wave and geometrical conditions, with various wave heights, bed slopes, and overhang sizes. Finally, conclusions are made in Section 4.

#### 2. Numerical modeling

All IHFOAM simulations have a two-dimensional (horizontal-vertical) geometry and use short duration solitary wave impacts. Hydrodynamic modeling assumes rigid, stationary, objects. Solitary waves are used to ensure computational expenses are feasible and numerical convergence is achieved. Because solitary waves are uniquely defined by their height to depth ratio, the results can be easily reproduced by other workers. Each simulation here takes approximately 8 h to run on 12 cores (Dual Six-core Intel Nehalem processors).

#### 2.1. RANS turbulence model

The full incompressible two phase RANS equations are solved using a standard  $k - \epsilon$  turbulence model (Greenshields, 2015) as implemented in the IHFOAM solver (IHCantabria, 2014). Shown in tensor form, the total stress for a turbulent Newtonian fluid,  $\overline{\sigma_{ii}}$ , is the combination of pressure stress, viscous stress, and Reynolds stress,

$$\overline{\sigma_{ij}} = -\bar{p}\delta_{ij} + \mu_f \left( \frac{\partial \overline{v_i}}{\partial x_j} + \frac{\partial \overline{v_j}}{\partial x_i} \right) - \overline{\rho v'_i v'_j}, \tag{1}$$

where  $\bar{p}$  is the pressure,  $\delta_{ij}$  is the Kronecker delta function, and  $\mu_f$  is the dynamic viscosity of a mixed

fluid, weighted by volume fraction y for water and air. The fluid velocity,  $v_i = \overline{v_i} + v'_i$  is composed of the Reynolds-averaged velocity  $\overline{v_i}$ , and turbulent fluctuating velocity,  $v'_i$ , and  $x_i$  denotes the three principal directions. The fluid density is given by  $\rho$ , and an overline denotes Reynolds averaging. The dynamic viscosity is defined as

$$\mu_f = \gamma \mu_{water} + (1 - \gamma) \mu_{air}, \tag{2}$$

where y = 0 for pure air and y = 1 for pure water.

Numerical tests performed here showed that the pressure stress is dominant in this problem at solid boundaries, accounting for greater than 99% of the magnitude of the total stress. Therefore, the approximation

$$\overline{\sigma_{ii}} \approx -\bar{p}\delta_{ii},$$
 (3)

can greatly reduce data needed in the calculation. Normal stresses on a surface, which are used here to compute loading, are then obtained directly from the model pressure outputs. Instantaneous forces on any face, for example, vertical forces on the overhang (or any other face), are computed from the spatial integrals of instantaneous pressure on that face. When this integration is performed at all time steps, it generates a time series of loading as shown in, for example, Figure 2.

#### 2.2. Model validation

The numerical model in this paper is validated with experimental data from Robertson et al. (2013), which examines horizontal forces on a vertical wall under solitary wave loading.

In Robertson's experiment, a solitary wave propagated over a 25.9m long flat bed, shoaled over a 28.5m long beach slope gaining 2.38m in elevation until reaching a 28.73 m long flat reef. The wave finally impacted a vertical wall at the end of the reef, and horizontal loads on the wall were recorded by four load cells at the structural supports. Instantaneous

loads experienced by the load cells in this experiment will differ to some degree from the integrated pressures computed on the wall face, even though both were measured at the same 1 kHz frequency. This is because the loads recorded at the structural supports are modified by the wall's mass and stiffness, while integrated pressures represent the actual applied loading. However, time integrals of loads and integrated pressures should match more closely. Details of the experimental setup may be found in Robertson et al. (2013), and data were found on the DesignSafe (www.design safe-ci.org) data warehouse.

Two simulations were reproduced with the numerical model and compared with Robertson's experiments: H = 0.133 m and H = 0.266 m. However, immediate challenges were found in simulation since the Robertson experiments did not generate a clean solitary wave as described by any theory. Figure 1 plots the surface elevation  $\eta$  at the beginning of the sloping bed, and demonstrates the irregular profile, particularly for the larger wave with nominal height H = 0.266 m.

Thus, the detailed form of the wave in the experiment could not be perfectly reproduced by the RANS model. Two solutions were employed: in the first, a solitary wave was generated using the nominal wave height for each experiment. This did not always give good results, particularly for larger waves, and the overall volume of water passing the gauge could be quite different between the laboratory and numerical experiments. Thus, a second solution was employed: in order to measure the total wave size, the second set of computations instead matched the integral of surface elevation over time, V, as

$$V(t_1, t_2) = \int_{t_1}^{t_2} \eta(t) dt.$$
 (4)

This overall integral was matched to a standard solitary wave solution; Goring's method was then used to generate a solitary wave from the boundary. Although

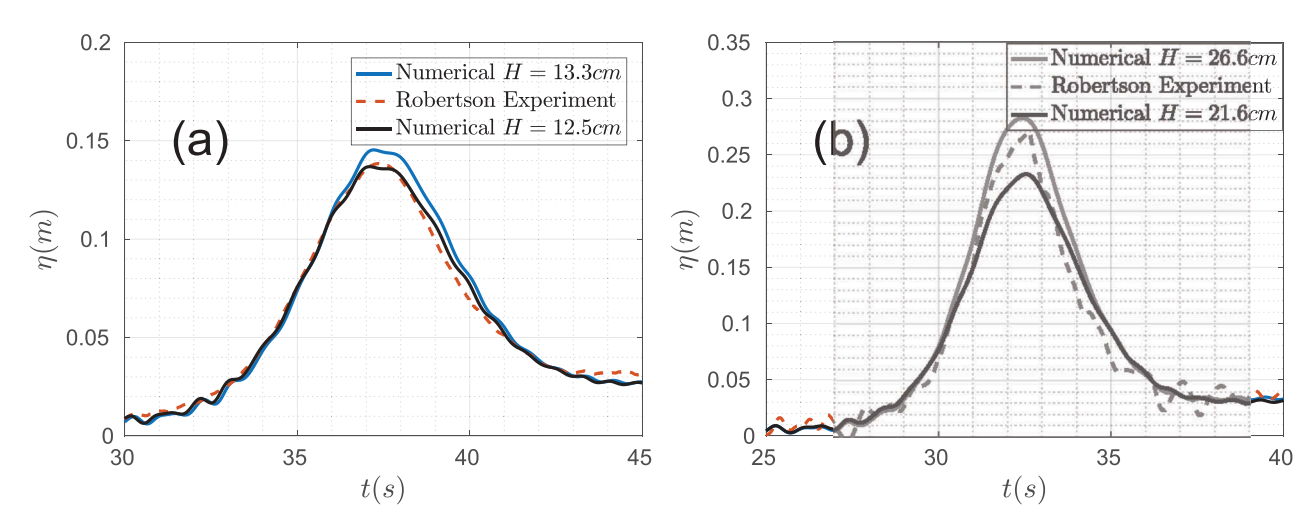


Figure 1. Surface elevation at position x = 25.9m (beginning of the sloping bed) for Robertson's experiments.

this did not provide perfect agreement to wave profiles, it gave a much better overall representation. However, some differences remained around the irregular peak, which affected to some degree details of the jet impact.

Figures 1(a) and 2(a) plot the water surface profiles at x = 25.9m, and the horizontal force on the vertical wall for the Robertson experiment with H = 0.133m, which was the smaller wave of the two tested. Surface elevations of the numerical model overlap with the experiment in Figure 1(a). Numerical results for H = 0.133m have a similar wave crest elevation but a slightly larger integrated wave size (0.92 m·s) than the Robertson experiment, which produced a wave size of 0.89 m·s. This laboratory integral was matched using a slightly smaller numerical wave with H = 0.125m. Both horizontal forces of the numerical simulations fit the experiment well except for the second peak around 46s. In addition, due to this single peak, the maximum horizontal force using our numerical model is 13% higher for H = 0.133m and 9% higher for H = 0.125m than was found in Robertson's experiment. Very clearly, instantaneous impact loads are very dependent on small-scale crest details; just as clearly, longer time scale loads are more dependent on integral properties of the wave.

The H = 0.266m solitary wave was also reproduced by the RANS model, and compared with Robertson's results as shown in Figures 1(b) and 2 (b). Here, the nominal wave height did not provide a good representation of the wave shape, and maximum force in the RANS simulation was 36% higher than experimental values. The overall loading was significantly higher at almost all times, not just near the peak, and the nominal wave height was clearly too large. After matching the time integral of surface elevation, a smaller solitary wave with amplitude H =0.216m was also generated and compared to laboratory results. The experimental surface elevations

show a slightly higher and narrower wave crest than the computational H = 0.216m wave, even though integral properties are matched; although the incoming wave does not follow any known wave theory and cannot be reproduced exactly, the overall volume is reproduced well. Figure 2(b) shows that the overall numerical forces from this H = 0.216m wave matched laboratory values very well, except around the second narrow peak at 49.5 s. Again, this peak force is very sensitive to details of wave breaking, and it is difficult to simulate without a perfect match of wave profiles.

#### 3. Simulations of solitary wave loading on a rectangular block

#### 3.1. Problem definition

Shallow water solitary waves are uniquely defined by their height to depth ratio  $H^* = H/h$ . They are also transient and well-suited to short simulations with high spatial and temporal resolution. Many studies have employed solitary waves as a first approximation to both storm waves and tsunamis (Briggs et al., 1995; Tadepalli and Synolakis, 1996; Kanoglu and Synolakis, 1998). The tests here will examine solitary wave loading on two-dimensional rectangular blocks with a range of incident waves and geometries.

Figure 3 defines the two-dimensional model used here: a rectangular block rests on top of a vertical wall, with the possibility of an overhang. We assume that the block adheres to the land tightly such that no air or water exists between the base of the block and the ground. The solitary wave height, static water level, and bed slope are given as H, h, and  $\beta$ , respectively. Faces 1–6 are marked on different walls, with  $x_i$ the length of each face. Waves are generated offshore, propagate toward the wall and, after impact with the wall, generate a vertical jet that provides loading to the elevated block.

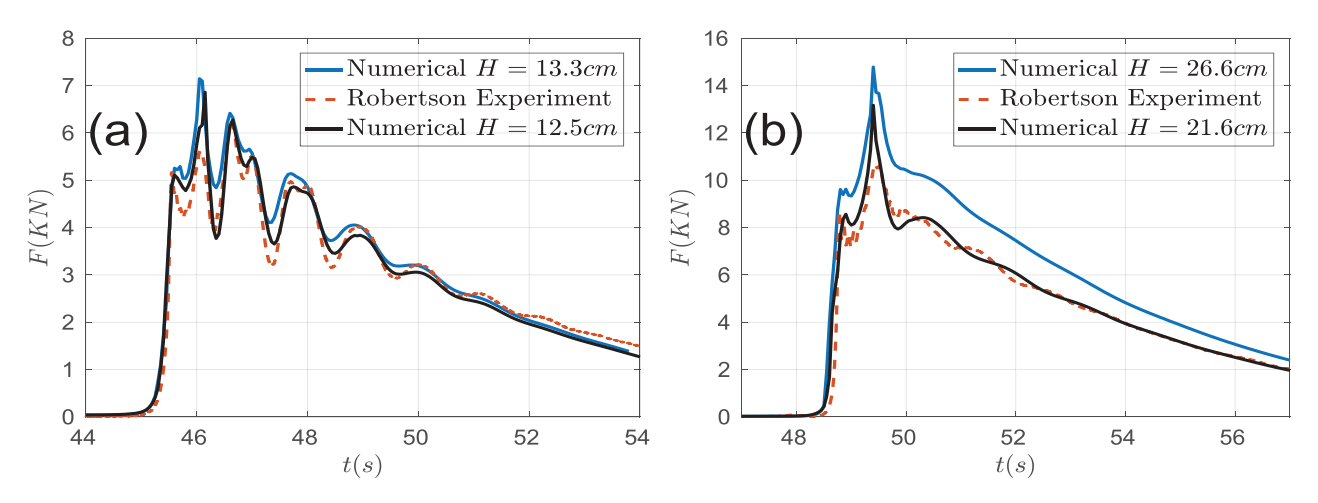


Figure 2. Validation of the numerical model by comparison with Robertson's experiment. Wave constants for the experiments are (a) H/h = 1/20, h = 2.66m, (b) H/h = 1/10, h = 2.66m. Standing water depth on the reef is 0.30m for both (a) and (b).

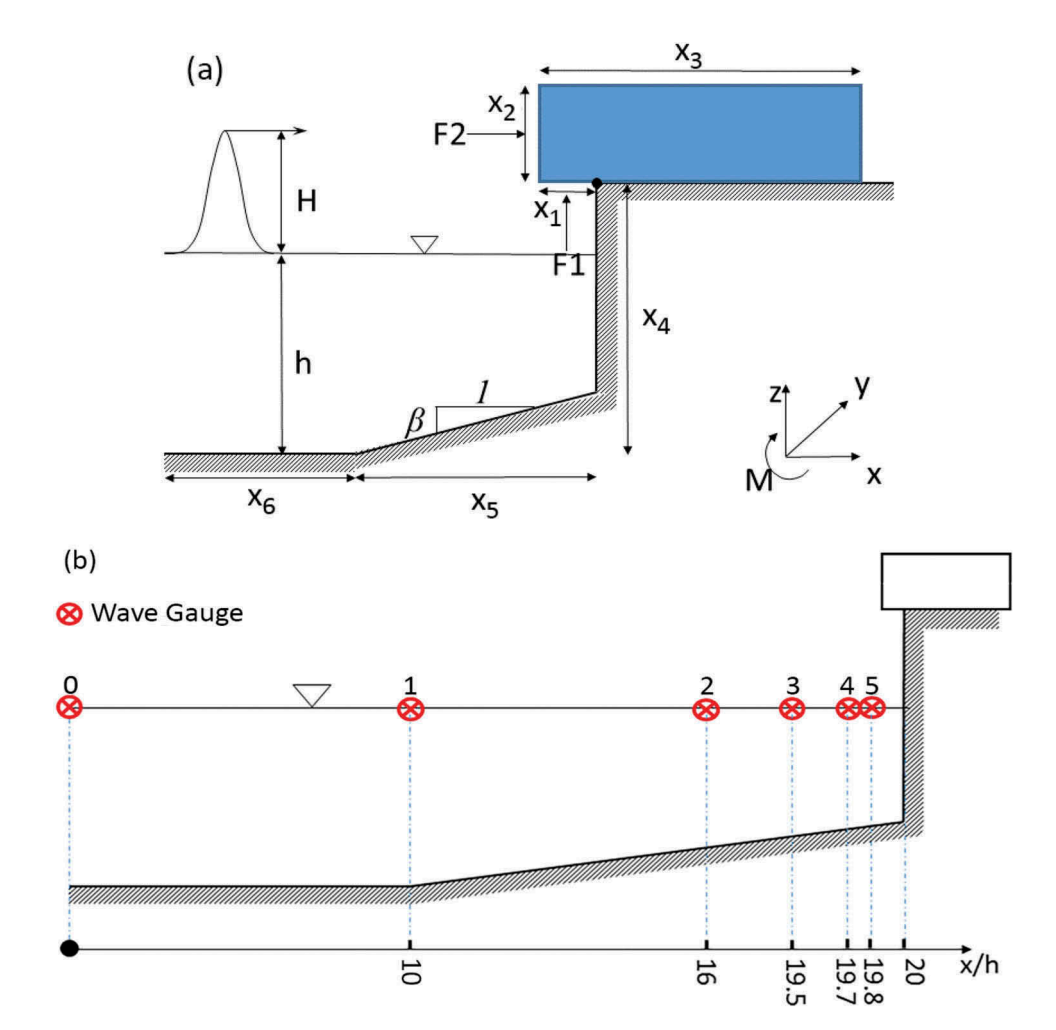


Figure 3. Definition sketch for model setup: (a) geometry and wave definitions; (b) locations of virtual wave gauges.

Table 2 gives the ranges of parameters used in the simulations. Again, important parameters varied during the experiments are dimensionless wave height  $H^*$ , length of the overhang  $x_1^*$ , wall height above the bed  $x_4^*$ , and bed slope  $\beta$ , with detailed parameters given in each section. Face lengths  $(x_2^*, x_3^*, x_5^*, x_6^*) = (0.5, 1, 10, 10)$  are kept constant over the course of the numerical experiments. Figure 3(b) shows positions for wave gauges where time series of water wave properties are recorded.

Solitary waves are implemented by IHFOAM according to the wave paddle theory of Goring and Raichlen (1980). The distance between the paddle and the sloping bed is  $x_6/h = 10$  so that any small re-reflections from the wave paddle will not have time to impact the block. The upper boundary of the simulation domain is set to be far from the breaking wave. The horizontal loading on Face 2 ( $F_2$ ) and vertical loading on Face 1 ( $F_1$ ) are functions of the solitary wave and geometrical properties, and are most significant for this study.

#### 3.2. Convergence verification

To ensure that computations provide an accurate solution to the defined problem, spatial and temporal convergence studies were performed using different numerical meshes and time steps. Results demonstrate

the degree to which solutions agree, and thus the accuracy of numerical results.

Before performing the convergence study, all parameters are made dimensionless, and 2D parameters are given per unit length (into the page). The normalized parameters are: time scale  $t^* = t/\bar{t}$ , length scale  $x_i^* = x_i/h$ , wave height  $H^* = H/h$ , pressure  $p^* = P/(\rho g h)$ , and force  $F^* = F/(\frac{1}{2}\rho g h^2)$ , where  $\rho$  is the density of water,  $\bar{t} = h/\sqrt{g h}$  is the time scale for a shallow water wave, and  $\frac{1}{2}\rho g h^2$  is the horizontal hydrostatic still water force. Taking h = 1 m and  $g = 9.81 m/s^2$ , the characteristic time scale,  $\bar{t}$ , is 0.319s.

Wave and geometric parameters used to test convergence are  $H^*=0.5$ ,  $x_1^*=0.1$ ,  $x_2^*=0.5$ ,  $x_3^*=1$ ,  $x_4^*=1.1$ ,  $x_5^*=10$ ,  $x_6^*=10$  and  $\beta=0$ . Convergence results for this single condition do not prove convergence for all test cases, but provide guidance into the choice of computational parameters and their accuracy.

#### 3.2.1. Spatial convergence

To investigate spatial convergence, four meshes were generated and tested as shown in Table 1. Mesh 1 is the coarsest, and subsequent Meshes 2–4 are obtained by (approximately) doubling the numbers of points in the previous grid.

Table 1. Spatial grid size.

	Mesh 1	Mesh 2	Mesh 3	Mesh 4					
(a) Overall grid size									
Total Grid Points	66,322	131,424	292,820	512,346					
$\delta s^*$	0.0378	0.0269	0.0180	0.0136					
(b) Normalized grid length ( $\delta s^*$ ) around overhang.									
Face 1	$3.45 \times 10^{-3}$	$2.56 \times 10^{-3}$	$1.69 \times 10^{-3}$	$1.27 \times 10^{-3}$					
Face 2	$2.94 \times 10^{-2}$	$2.00  imes 10^{-2}$	$1.32 \times 10^{-2}$	$1.00 \times 10^{-2}$					
Face 3	$2.50\times10^{-2}$	$1.89\times10^{-2}$	$1.27\times10^{-2}$	$9.43\times10^{-3}$					

Table 2. Parameter list for simulations. In each row, all combinations of parameters are used.

H*	<i>x</i> <sub>1</sub> *	<i>x</i> <sub>2</sub> *	<i>X</i> <sub>3</sub> *	<i>X</i> <sub>4</sub> *	<i>x</i> <sub>5</sub> *	<i>x</i> <sub>6</sub> *	β
0.5	0.1	0.5	1.0	(1.1:0.1:2.5)	10	10	(0,0.05,0.1)
				(1.1 : 0.1 : 2.5)			
0.5	(0:0.05:0.2)	0.5	1.0	(1.1:0.1:2.5)	10	10	0.05
0.6	(0:0.05:0.2)	0.5	1.0	(1.1:0.1:2.5)	10	10	0.05

A characteristic length scale for the overall spatial resolution is calculated using

$$\delta s = \frac{\sqrt{A_D}}{\sqrt{N_G} - 1},\tag{5}$$

where  $A_D$  is the area of the computational domain and  $N_G$  is the number of grids; normalization is then  $\delta s^* = \delta s/h$ . Forces acting on the overhang are the most important, and the resolution is much finer on Faces 1–3 as shown in Table 1(b) and Figure 4. The normalized time step used here is  $\delta t^*$  is 15.7  $\times$  10<sup>-4</sup>, and temporal convergence will be validated in the subsequent section.

Pressures and forces are sampled everv 0.005s (normalized  $t^* = 0.0157$ ) for both the convergence verification shown here and all wave load analyses. Peak loads on Face 1 (vertical force on underside of block) are shown in Figure 5 and vary by less than 2% between the coarsest and finest meshes, while Face 2 (horizontal force on vertical side of block) shows a 3% variation in peak forces.

Between the two finest meshes, peak forces on the two faces differ by less than 1%. At much later times  $(t^* = 28 - 30)$ , some variation occurs which appears to be related to the details of splashing, but peak forces show good convergence. Therefore, based on these results, simulations will use the finest Mesh 4 (and equivalently sized meshes for other geometries) for all remaining tests.

#### 3.2.2. Temporal convergence

Temporal convergence is examined for Mesh 4 by setting the normalized time step  $\delta t^* = (7.8, 15.7, 31.3) \times 10^{-4}$ . Again, forces along Face 1 and 2 are plotted in Figure 5(c-d). Peak loads for all time steps tested are almost identical, demonstrating temporal convergence for this problem. Based on these results, the intermediate time step  $\delta t^* = 15.7 \times 10^{-4}$  is applied in this study in concert with Mesh 4.

#### 3.3. Loading example

Figure 6(a) shows the time series of water surface elevation at locations shown in Figure 3(b) using  $(H^*, x_1^*, x_4^*, \beta) = (0.5, 0.1, 1.1, 0.05)$ . This represents a large wave impacting a low overhanging block with  $x_4^* = 1.1$ , that is, the base of the block is 0.1 water depths above the still water level. A gradual shoaling takes place as the solitary wave propagates into more shallow water. As the wave impacts the wall, it is near-breaking and generates a strong vertical wall jet, greatly increasing near-wall surface elevations. These large water surface elevations generate correspondingly large horizontal and vertical forces on the overhanging block, shown in Figure 6(b). Both forces are nondimensionalized by the horizontal hydrostatic force  $\frac{1}{2}\rho gh^2$ , meaning that all forces here may be considered in terms of equivalent reference

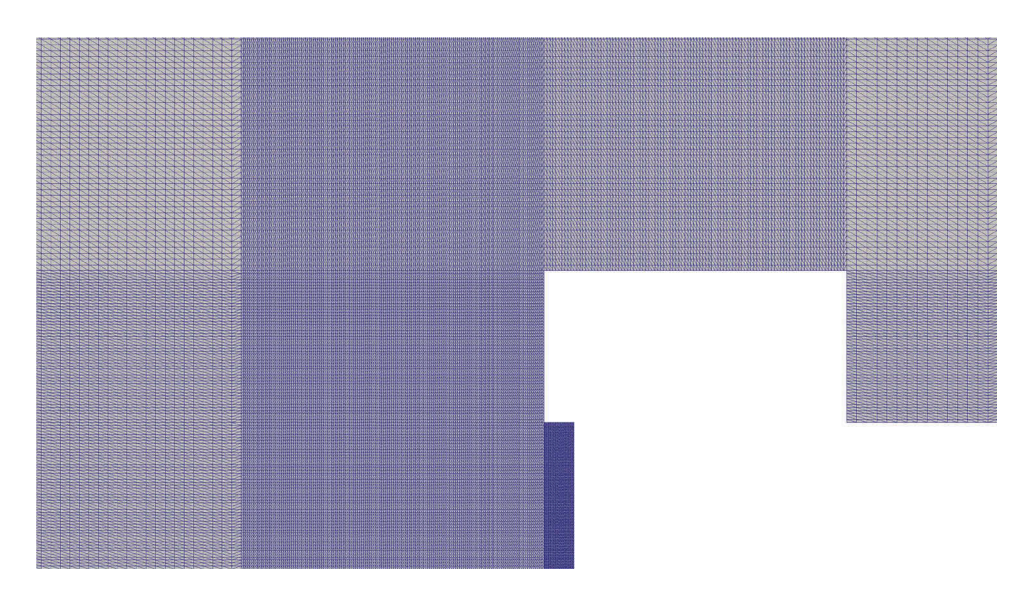


Figure 4. Closeup of computational mesh around overhang, showing areas of refinement.



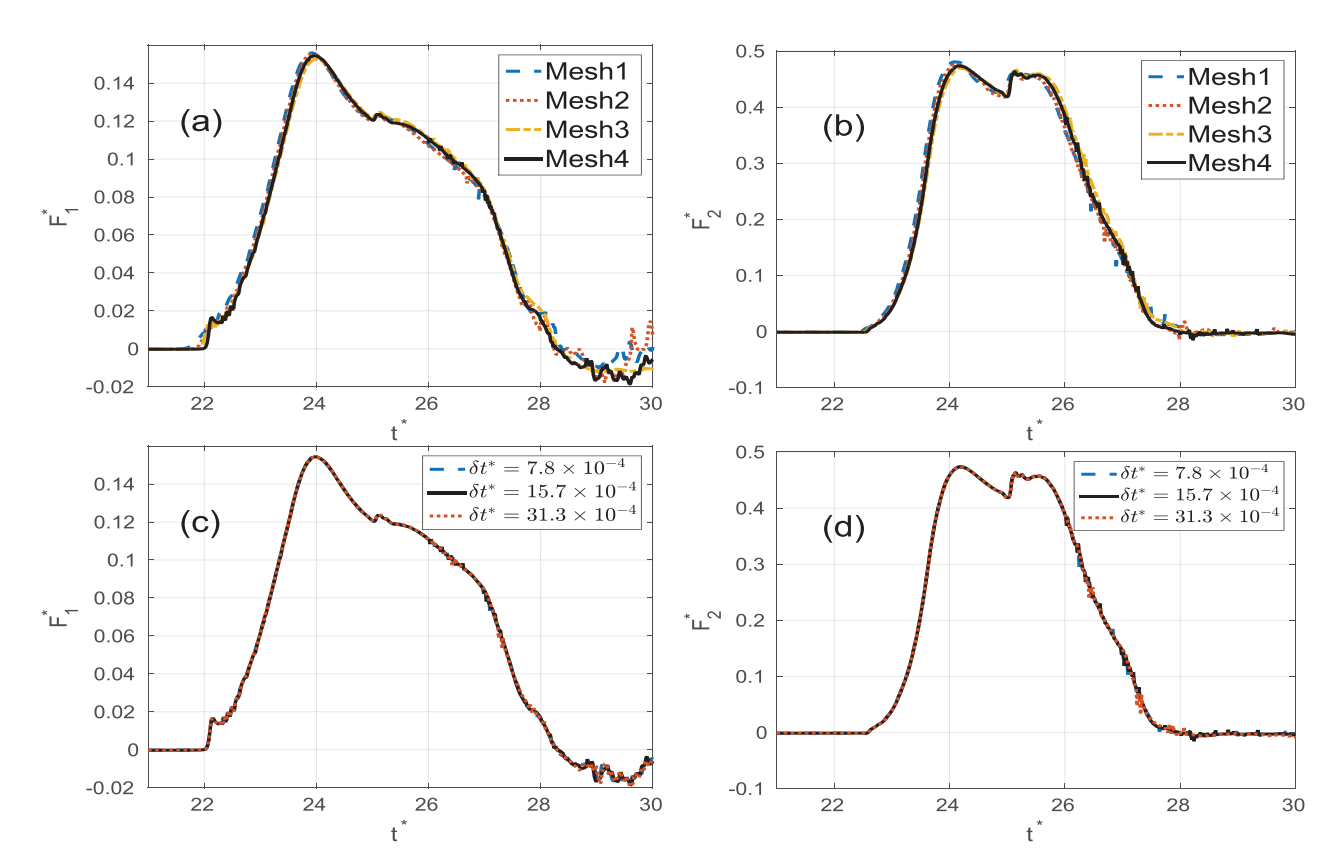


Figure 5. Time series of  $F_1^*$  and  $F_2^*$  for convergence study. Subplots (a) and (b) show spatial convergence, subplots (c) and (d) show temporal convergence. Wave and geometry parameters for this convergence study are  $(H^*, x_1^*, x_4^*, \beta) = (0.5, 0.1, 1.1, 0)$ .

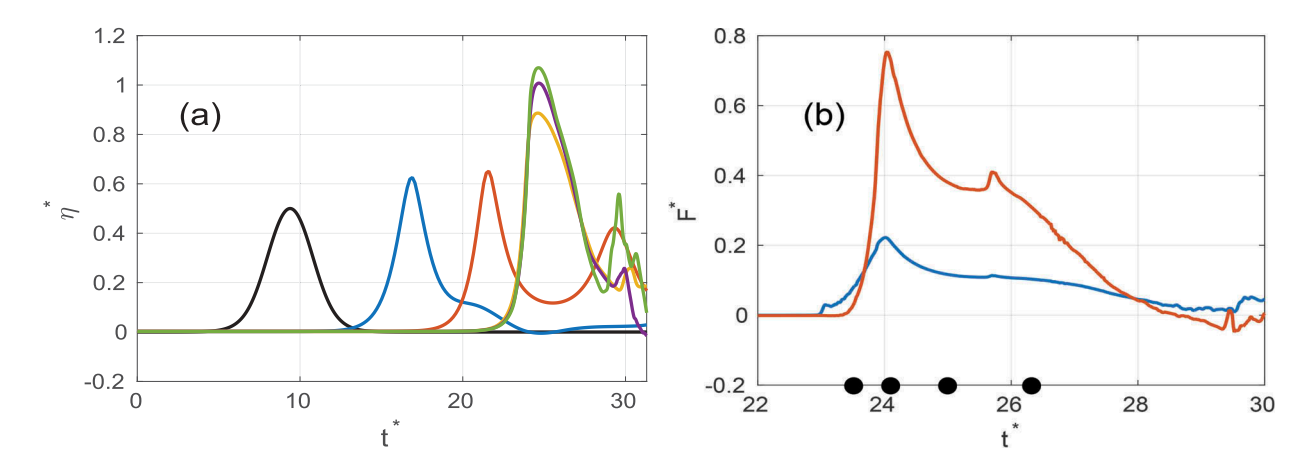


Figure 6. Time series for (a) water elevation at Gauges 0-5; Gauge 0 (black); Gauge 1 (blue); Gauge 2 (red); Gauge 3 (yellow); Gauge 4 (purple); Gauge 5 (green). (b) Integrated forces  $F_1^*$  (blue) and  $F_2^*$  (red), showing times of snapshots in Figure 7.

hydrostatic loads. The peak horizontal load on the elevated block is  $F_2^* = 0.75$ , and the vertical uplift load for  $x_1^* = 0.1$  length overhang has a much lower peak of  $F_1^* = 0.22$ . The peak horizontal load has a short duration, decreasing to about half its value over a time  $\delta t^* \approx$  1. Vertical loads show a somewhat smaller relative reduction. Short duration impulsive loads are known to occur for near-breaking or breaking-waves on vertical structures (Peregrine, 2003; Shafiei, Melville, and Shamseldin, 2016), and are followed by longer duration quasi-static loads.

Figure 7 shows snapshots of solitary wave impact on the block for the same conditions shown in Figure 6. This wave sequence explains the loading properties in Figure 6(b), and demonstrates why horizontal loads on Face 2 begin to increase after vertical loads on Face 1. Both peak loads occur before splashing impacts the top face of the block (Face 3). A strong jet overtops both the wall and the block, and could generate large forces on near-coast inland regions.

#### 3.4. Time averaged loading analysis

Peak forces in Figure 6(b) can have a relatively short duration, but lower levels of loading continue for a significantly longer time. It is well known in structural

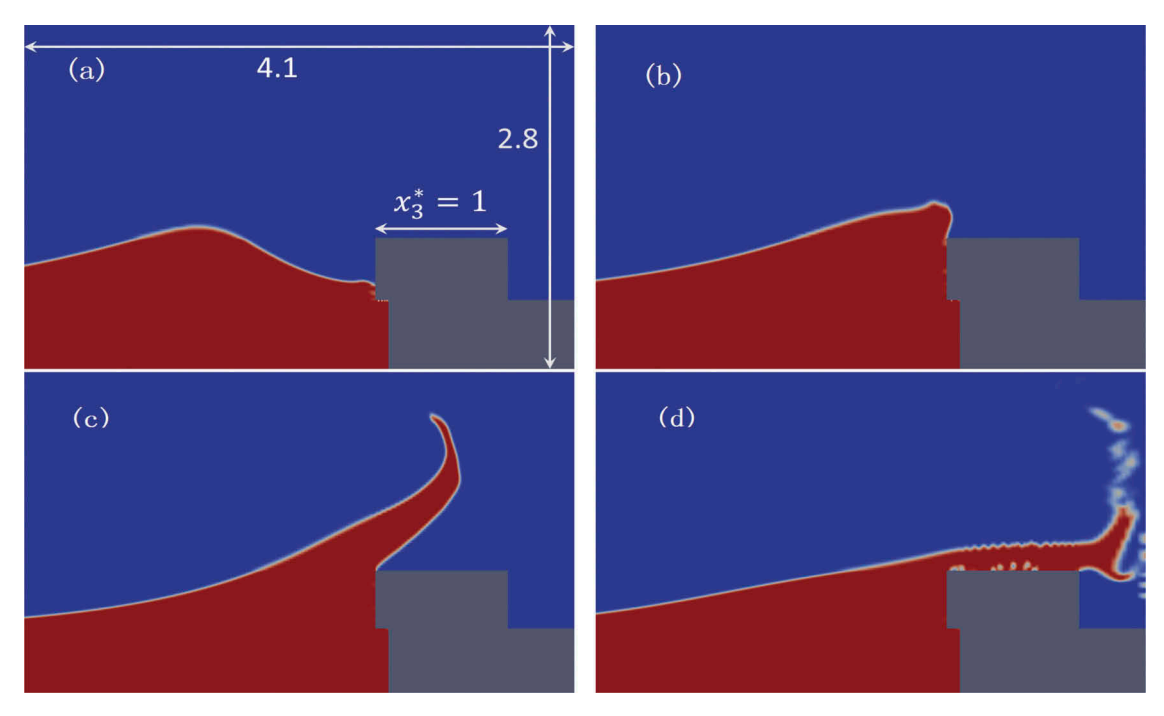


Figure 7. Sequence of water surfaces for wave breaking, using geometries  $(H^*, x_1^*, x_4^*, \beta) = (0.5, 0.1, 1.1, 0.05)$ . (a)  $t^* = 23.5$ , (b)  $t^* = 24.1$ , (c)  $t^* = 25.1$ , (d)  $t^* = 26.3$ .

engineering that different structural modes and failure mechanisms respond at different time scales. As one example, failure of a timber-framed wall under wave action may occur almost instantaneously under breaking wave loading (Tung et al., 1999), demonstrating response at very short time scales; here, the maximum instantaneous force may be appropriate for loading analysis. In contrast, a steel moment-framed building may not respond to these slamming modes but instead to wave loading scales long enough that static pushover analysis becomes more appropriate (Attary et al. 2013). If the instantaneous maximum load were applied to this case, it would clearly overestimate the likelihood of failure.

However, despite the knowledge that different loading durations are applicable in different situations, there has been very little study on how wave forces vary with loading duration. Peregrine (2003) studied short duration forces by considering the pressure-impulse, calculated by integrating the forces over the time duration of wave impact. The impulse was noted to be more reproducible than peak forces when measuring wave impacts on structures, but there was little investigation of duration effects. For this study, we will also examine integrated time-averaged loads and impulse, which are directly related. Loads averaged over time scale  $\Delta t^*$  are considerably lower than peak loads, but may be more applicable to structural design. The maximum load over an averaging time scale  $\Delta t^*$  is defined as

$$F_{\max}^*(\Delta t^*) = \frac{1}{\Delta t^*} \max \left( \int_{t^* - \frac{1}{2} \Delta t^*}^{t^* + \frac{1}{2} \Delta t^*} F^*(t^*) dt^* \right). \tag{6}$$

or as the maximum instantaneous load for  $\Delta t^* = 0$ . Thus, for any loading event and averaging period  $\Delta t^*$ , we find the time interval where this averaged load is maximum and record the magnitude. The maximum pressure-impulse over time scale  $\Delta t^*$  is then simply  $\Delta t^* F_{\text{max}}^* (\Delta t^*)$ .

Figure 8 plots the time averaged vertical force  $F_{1,max}^*(\Delta t^*)$  and horizontal force  $F_{2,max}^*(\Delta t^*)$  for averperiods  $\Delta t^* = (0, 1/20, 1/10, 1/5, 1/2.5, 1)$ along wall heights  $x_4^* = 1.1 - 2.5$ . Results for  $H^* =$ 0.5 are given in Figure 8(a-b) and  $H^* = 0.6$  in Figure 8(c-d). Tests in this section have a moderate slope  $\beta = 0.05$ , and an overhang length  $x_1^* = 0.1$ . Horizontal and vertical loads show quite different patterns. Instantaneous vertical loads on the overhang  $(F_1^*)$  are very low for low wall heights and increase significantly as wall elevations  $(x_4^*)$  increase. This result occurs because the jet has not yet fully developed at low elevations. For  $H^* = 0.5$ , the maximum load of  $F_1^* = 1.90$  occurs at  $x_4^* = 1.8$  (i.e. the bottom of the block is 0.8 water depths above still water level), which is considerably higher than the initial solitary wave crest elevation of  $H^* = 0.5$ . This wave is nearbreaking on the wall and develops a strong vertical jet as described by, for example, Peregrine (2003). Vertical loads decrease as wall height increases above  $x_4^* = 1.8$  but remain significant. However, vertical loads decrease strongly with increased averaging time to a near-constant  $F_1^*(0.4) = 0.2 - 0.25$ , and  $F_1^*(1) = 0.1 - 0.15$ , indicating that peak vertical loads occur on short time scales. Interestingly, for the longest averaging period of  $\Delta t^* = 1$ , the maximum time averaged vertical load is slightly larger for

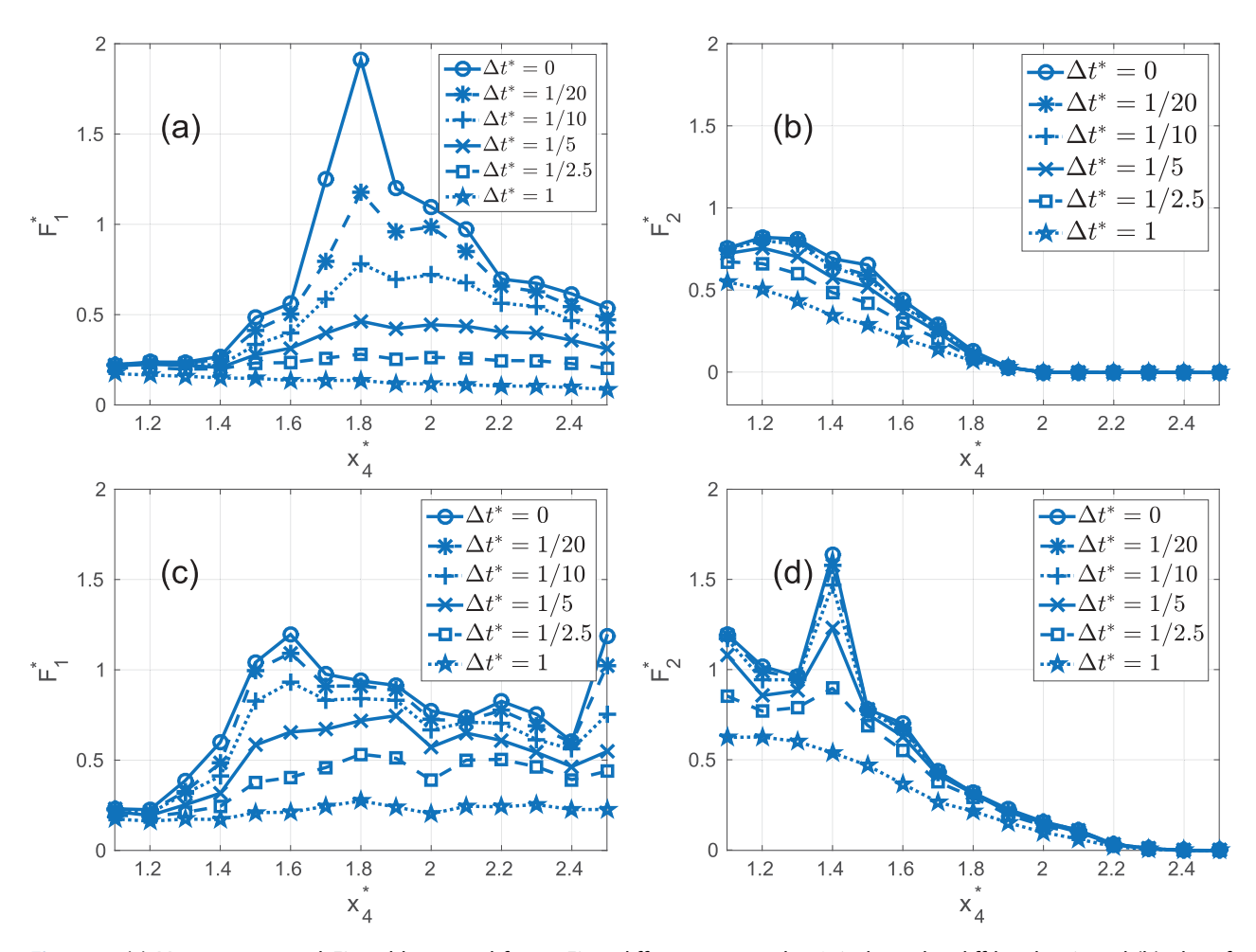


Figure 8. (a) Maximum vertical  $F_1^*$  and horizontal forces  $F_2^*$  at different time scales  $\Delta t^*$  along the cliff height  $x_4^*$ , and (b) plot of the maximum vertical and horizontal forces for  $H^* = 0.5$ . (c) and (d) are as in (a) and (b) with  $H^* = 0.6$ . Wave and geometry constants are  $(x_1^*, x_4^*, \beta) = (0.1, 1.1 : 0.1 : 2.5, 0.05)$ .

low wall heights than for the higher elevations that give a much larger instantaneous load. This total impulse may be larger for low elevations because of the much longer contact time between the wave and the block underside when compared to the highly transient jet found at high elevations.

For the larger wave with  $H^* = 0.6$ , a similar increase in  $F_1^*$  is seen as wall height  $x_4^*$  increases, but there is an irregular decrease from the peak value of 1.2, showing considerable volatility. These peak values are actually smaller than those that were found with the smaller wave,  $H^* = 0.5$ , almost certainly because the larger wave broke earlier and did not produce as strong as a jet as the smaller wave. However, timeaveraged vertical loads ( $\Delta t^* > 1/5$ ) are much larger for the larger wave height  $H^* = 0.6$ , reflecting the longer duration of loading and a greater volume of water passing the overhang. Maximum loads for  $\Delta t^* = 1$  are almost constant with block elevation, suggesting a strong insensitivity to block height when compared to instantaneous loads.

Horizontal loads  $(F_2^*)$  show maxima at much lower wall elevations  $(x_4^*)$  for both wave heights tested here, and show a strong reduction in loads for very large wall elevations. This appears to be because the

vertical jet, which provides the greatest loading at high elevations, does not produce large horizontal velocities; in contrast, the main wave just before wall impact has large horizontal velocities that lead to correspondingly large horizontal loads at lower block elevations. With one exception, horizontal loads have a very weak dependence on the time averaging period, indicating that horizontal impacts have a much longer duration, as would be expected if the solitary wave is being partially reflected. This single exception, at wall height  $x_4^* = 1.4$  for  $H^* = 0.6$ , shows a very large peak horizontal load of  $F_2^* = 1.6$ , and appears to arise from very fine scale details of wave slamming against the block at this elevation. Interestingly, although the instantaneous load from this block elevation is much larger, the longest time averaged period with  $\Delta t^* = 1$  retains no trace of this spike, showing that it was quite short-lived. Overall, peak vertical loads are of similar or greater magnitude to peak horizontal loads. Although both horizontal and vertical peak loads can exceed reference hydrostatic forces, only vertical loads continue to be important at higher elevations. Finally, horizontal loads tend to be more significant for longer averaging periods.



#### 3.5. Bed slope effects

The importance of bed slope arises from its effect on wave breaking: as the bed changes from flat to sloping, there is a significantly greater tendency for waves to break either before or at the wall. Figure 9 plots wave elevation for  $x_4^* = 1.1$  at wave Gauge 5 (0.2h from wall) using  $\beta = (0, 0.05, 0.1)$ . For both wave heights  $H^* = (0.5, 0.6)$ , the maximum water surface elevation is largest for the zero slope bathymetry. Breaking with bore formation is evident for larger

slopes. However, this breaking does not mean that forces decrease.

Figure 10 plots maximum instantaneous forces  $F_1^*$ and  $F_2^*$  as a function of wall elevation  $x_4^*$  for slopes  $\beta = (0, 0.05, 0.1)$ . Slope strongly influences maximum loads, with maximum vertical forces increasing as bed slope increases, particularly for the smaller wave height,  $H^* = 0.5$ . Maximum instantaneous horizontal and vertical loads for both  $\beta = 0.05$  and  $\beta = 0.1$ exceed the reference still water hydrostatic forces,

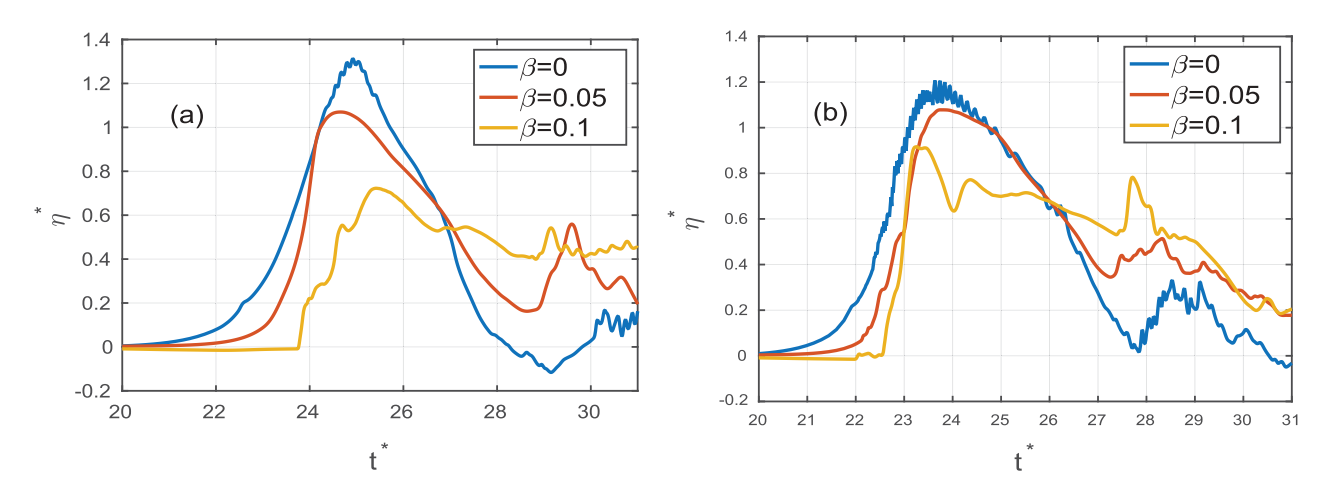


Figure 9. Time series for water elevation at wave Gauge 5 for bed slope  $\beta = (0:0.05:0.1)$ , with (a)  $H^* = 0.5$ , and (b)  $H^* = 0.6$ . Other geometric constants used here are  $(x_1^*, x_4^*) = (0.1, 1.1)$ .

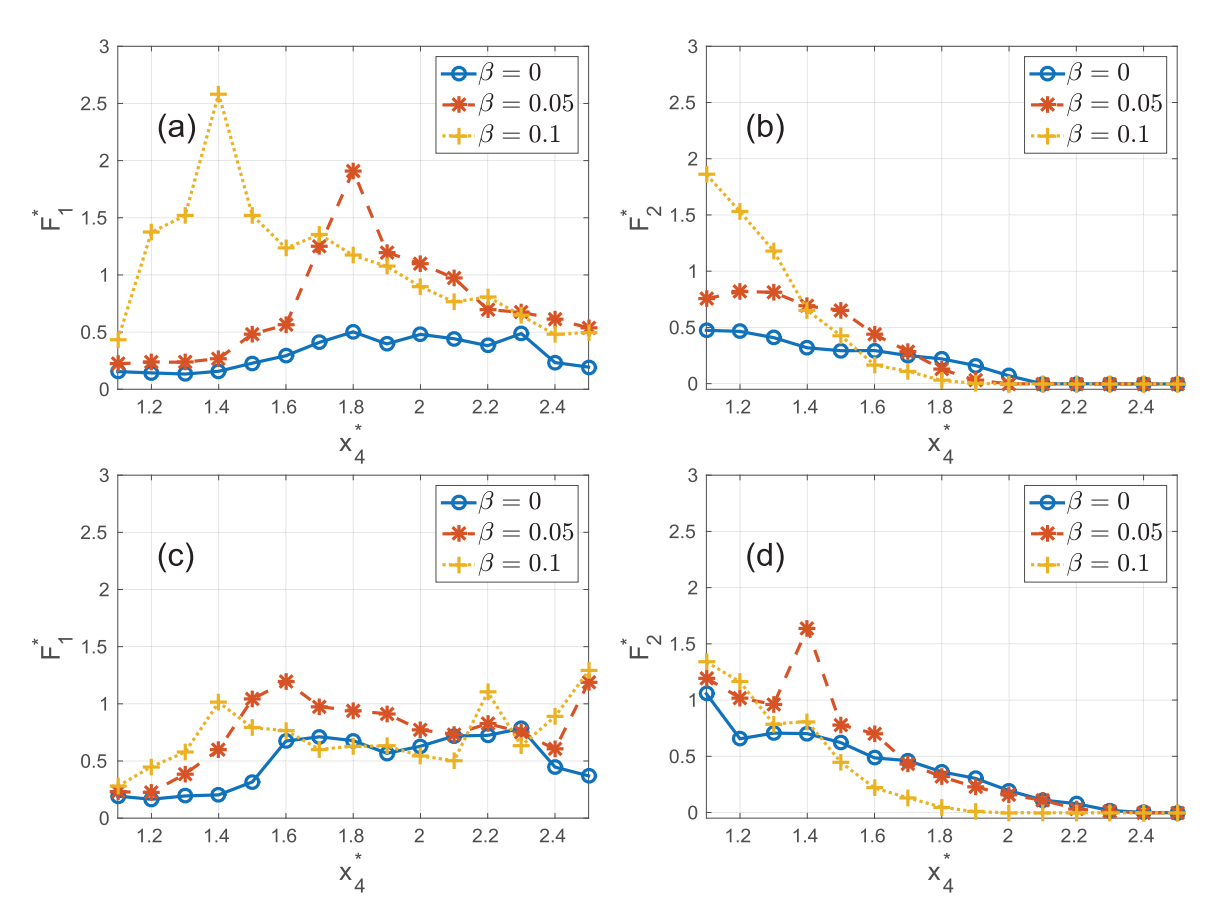


Figure 10. Maximum instantaneous ( $\Delta t^* = 0$ ) vertical  $F_1^*$  and horizontal  $F_2^*$  forces at bed slopes  $\beta = (0:0.05:0.1)$  along block elevation  $x_4^* = 1.1 - 2.5$ . (a) and (b) plot the vertical and horizontal forces for  $H^* = 0.5$ , (c) and (d) are for  $H^* = 0.6$ . Length of overhang here is  $x_1^* = 0.1$ .

but loads for flat beds do not. Again, this clearly indicates that breaking or near-breaking conditions at the wall may significantly increase wave-induced forces.

When loads are averaged over time, maximum forces decrease but can still remain large, particularly for sloping beds. Figure 11 shows the maximum time-averaged horizontal and vertical loads for slopes with time averaged periods  $\Delta t^* = (0, 1/20, 1/10, 1/5, 1/2.5, 1)$ . The maximum vertical forces for each of the three slopes in Figure 10(a) are found for  $\Delta t^* = 0$  in Figure 11(a). As averaging periods increase, vertical loads decrease quite rapidly; although vertical loads can have large instantaneous magnitudes, they are of relatively short duration. Horizontal loads also decrease, but at a slower rate, and some remain almost constant for longer averaging periods. All simulations show that loads are lowest for flat beds, and tend to increase as bed slope increases. However, this increase is not monotonic, and likely depends on breaking details that are difficult to determine a priori.

#### 3.6. Overhang effects

Simulations were performed using overhang lengths  $x_1^* = (0, 0.05, 0.1, 0.15, 0.2)$  with intermediate bed slope  $\beta = 0.05$  and wave heights  $H^* = (0.5, 0.6)$ . Figure 12 shows surface elevations at Gauge 5 for both

wave heights. No differences are seen for any overhangs until near the wave peak. Here, increasing the overhang size results in a modest increase in the maximum water levels, likely because water is redirected toward Gauge 5, which is 0.2h away from the wall.

Figure 13 plots maximum instantaneous forces  $F_1^*$ and  $F_2^*$  as a function of wall elevation  $x_4^*$  for overhang lengths  $x_1^* = 0 - 0.2$ . Panels (a–b) give results for  $H^* =$ 0.5 and panels (c–d) show results for  $H^* = 0.6$ . The first observation is that overhangs strongly increase peak vertical loads on a block, while they have small effects on the horizontal loads. The increase in vertical loads with overhang length is expected, as increasing overhang length increases the area over which vertical forces can act. Peak vertical loads can be extremely large, and forces exceed four times the reference hydrostatic value for the smaller wave height  $H^* =$ 0.5 at wall elevations  $x_4^* = 1.8 - 1.9$ . Loads for the larger wave height,  $H^* = 0.6$ , show a much broader peak of high loads at different elevations but never reach the large peaks found for the smaller wave height. These differences in peak loads appear to be related to small differences in wave breaking at the wall, which can have strong influences on the vertical wall jet (e.g. Peregrine, 2003).

In contrast to vertical forces, horizontal loads show weak dependence on overhang length. Peak loads vary by less than 10% with increasing

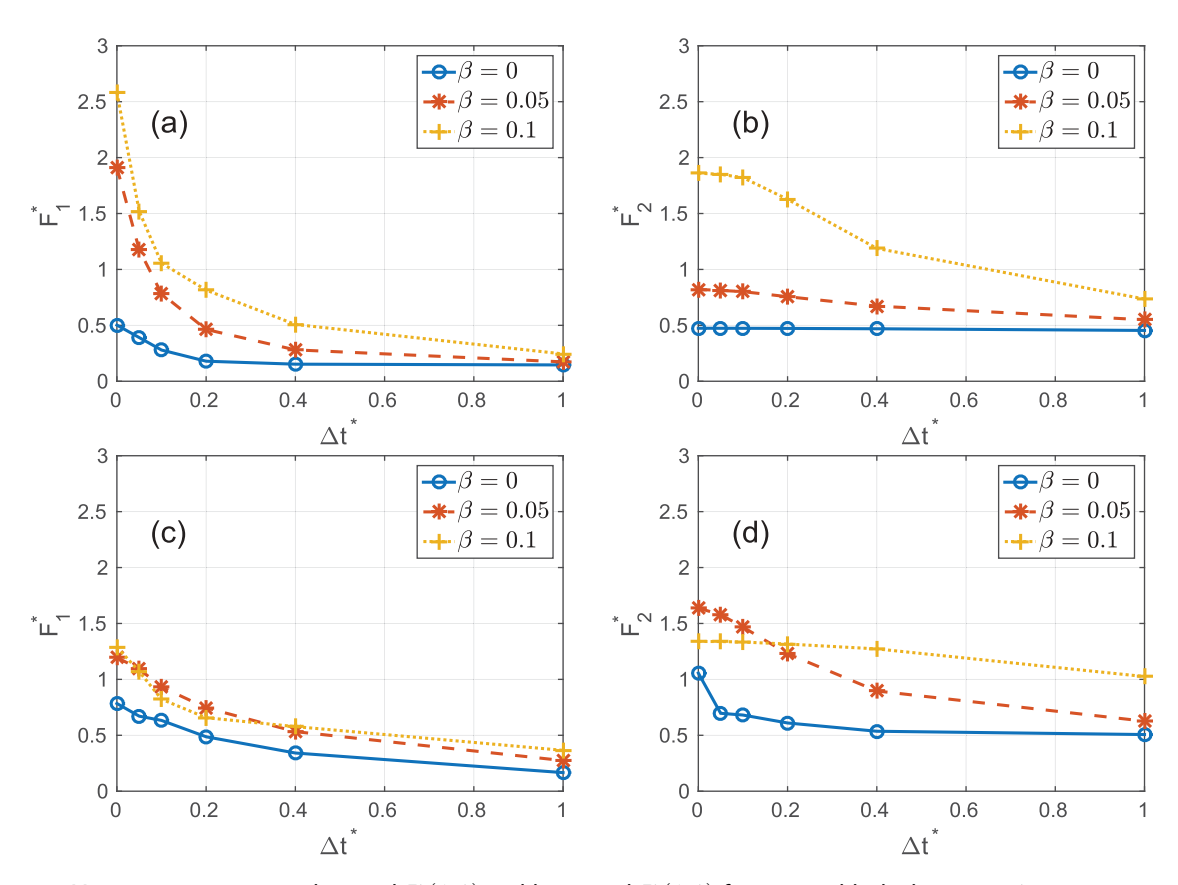


Figure 11. Maximum time averaged vertical  $F_1^*(\Delta t^*)$  and horizontal  $F_2^*(\Delta t^*)$  forces over block elevations  $x_4^* = 1.1 - 2.5$  at bed slopes  $\beta = (0:0.05:0.1)$ . (a) and (b) plot the vertical and horizontal forces for  $H^* = 0.5$ ; (c) and (d) are for  $H^* = 0.6$ . Length of overhang here is  $x_1^* = 0.1$ .

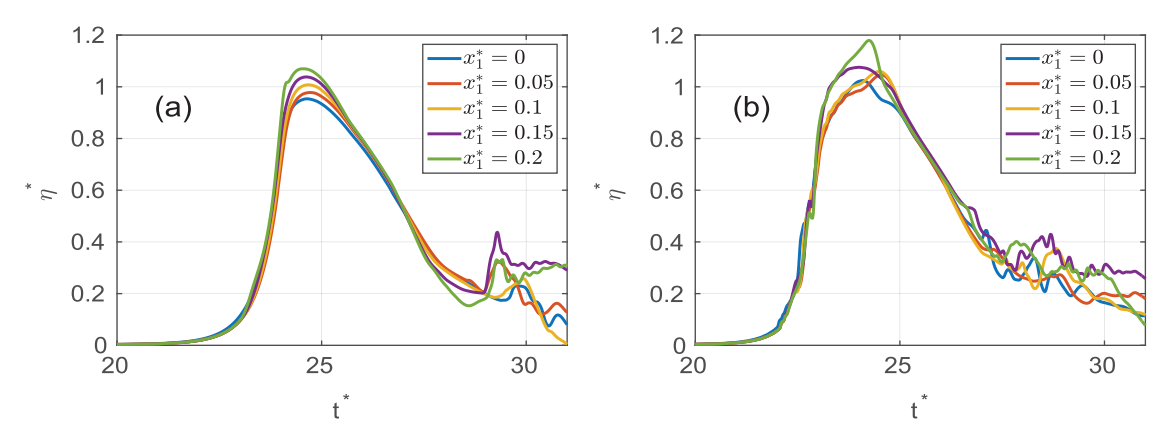


Figure 12. Time series for water elevation at wave Gauge 5 for (a)  $H^* = 0.5$  and (b)  $H^* = 0.6$ . Geometric constants used here are  $(x_4^*, \beta) = (1.1, 0.05)$ .

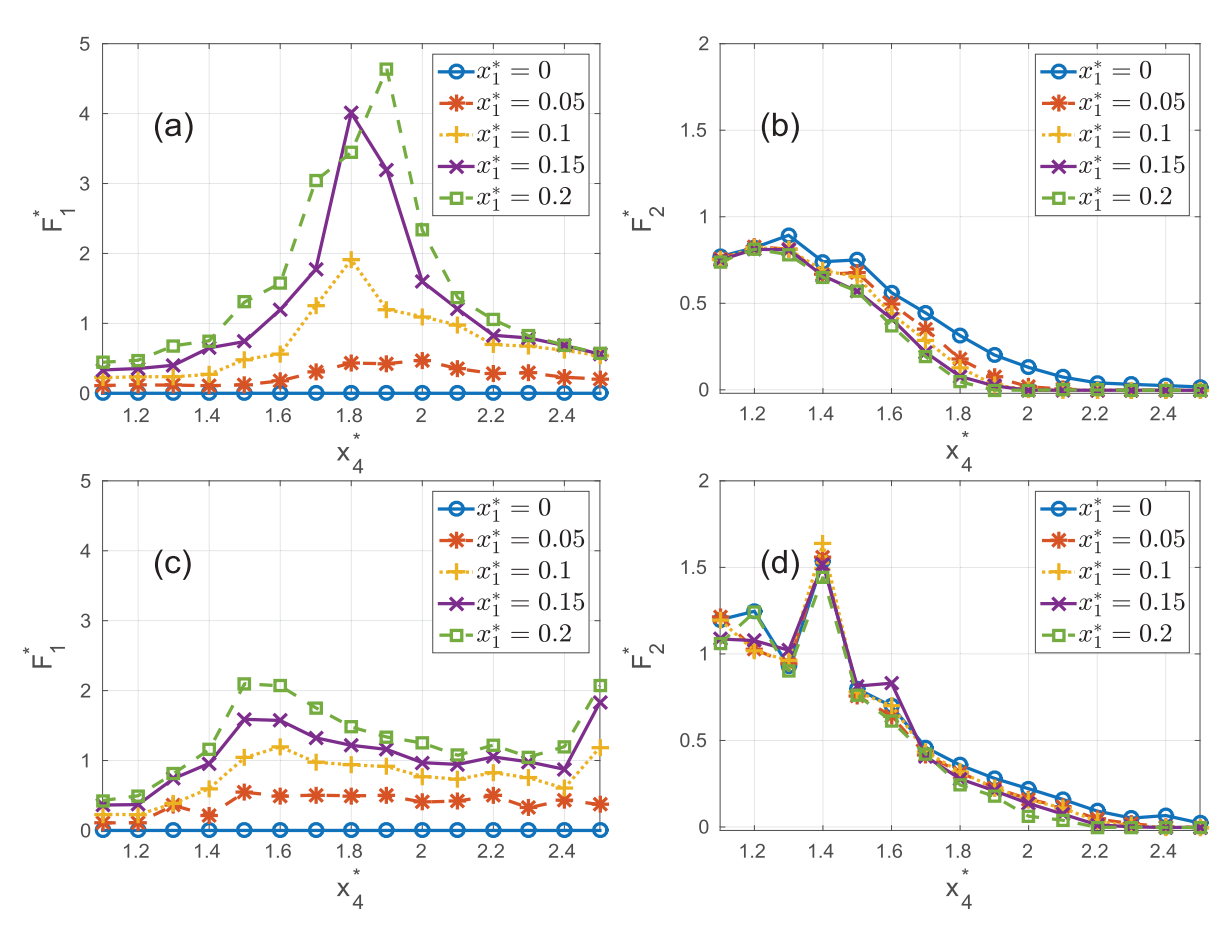


Figure 13. Maximum vertical  $F_1^*$  and horizontal  $F_2^*$  forces for various overhang lengths  $x_1^*$  along block elevation  $x_4^* = 1.1 - 2.5$ : (a) vertical and (b) horizontal forces for  $H^* = 0.5$ ; (c) and (d) for  $H^* = 0.6$ . Bed slope  $\beta = 0.05$ .

overhang length, and they have no qualitative changes; again, the small dependence on overhang length is not surprising since face area  $x_2^*$  is not changed. There are some differences at higher elevations, as it may be more difficult for the jet to redirect around the overhang and impact the vertical face, and a larger overhang here leads to lower horizontal loads. However, the robustness of horizontal loads to details of the overhang is beneficial for geometric predictions that may not correspond perfectly to the idealized scenarios given here. Different from vertical loads, horizontal loads have

maxima at lower wall elevations, and decrease to near-zero for high walls.

Time averaging, as introduced previously, simplifies loading in many ways as shown in Figure 14. The high-magnitude, short-duration vertical peak loads decrease strongly for both wave heights as averaging time increases. Although there remains a strong dependence on overhang length  $x_1^*$ , by an averaging period of  $\Delta t^* = 0.4$ , all dimensionless vertical loads are less than the reference hydrostatic force, and show large decreases from their peaks. Vertical loads  $H^* = 0.5$ for decrease particularly rapidly,

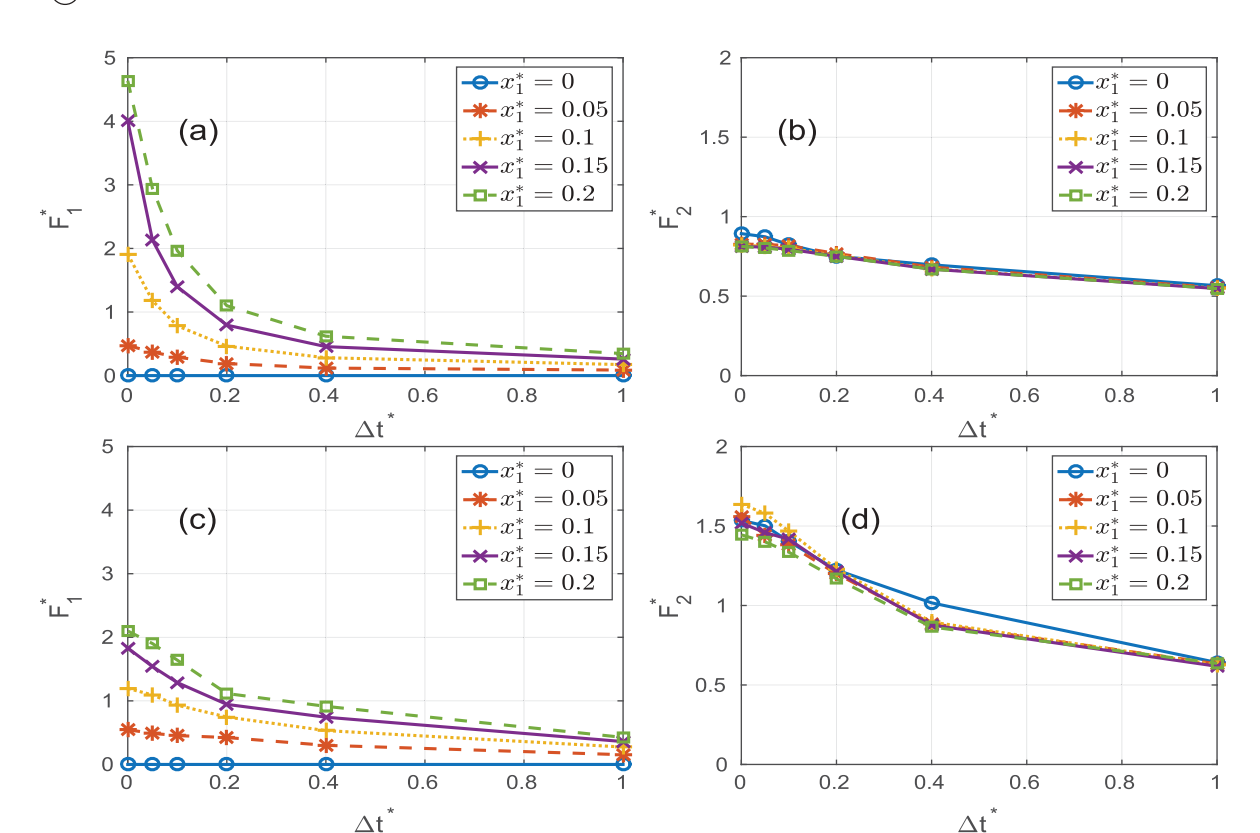


Figure 14. Maximum time averaged vertical  $F_1^*(\Delta t^*)$  and horizontal  $F_2^*(\Delta t^*)$  forces for all block elevations  $x_4^* = 1.1 - 2.5$  at various overhang lengths  $x_1^*$ . (a) and (b) plot the vertical and horizontal forces for  $H^* = 0.5$ ; (c) and (d) are for  $H^* = 0.6$ . Bed slope here is  $\beta = 0.05$ .

demonstrating that although vertical jets may induce large forces, they do not provide sustained impacts.

In contrast, horizontal loads show a much weaker, though non-negligible, dependence on averaging time. For the largest averaging period,  $\Delta t^* = 1.0$ , time-averaged horizontal loads on Face 2 are larger than the time-averaged vertical loads on Face 1 even though instantaneous vertical loads were much larger.

Accumulated evidence for the weak dependence on the overhang length seen here and in Figure 13 demonstrates the robustness of horizontal loading. This is because the momentum-conservation arguments constrain the momentum impulse required to decelerate and reflect the solitary wave; however, corresponding arguments for the vertical loads are much more dependent on the details of the vertical jet.

#### 4. Discussion and conclusions

This paper presents a numerical study for solitary wave loads on overhanging near-coast structures. In common with other reports, this study showed that nearbreaking and breaking waves generate the largest loads. Conceptually, the system here may be considered as having two parts: a partially reflected solitary wave that acts mainly on the lower portion of the wall, and a vertical jet that reaches much higher elevations.

The solitary wave has large horizontal velocities before the wall but lower vertical velocities; at low block elevations this leads to large horizontal pressures and forces but low vertical loads. These high pressures are what develop the vertical jet, which reaches its greatest strength at higher elevations where it has large vertical velocities but low horizontal velocities. With this conceptual system in mind, vertical loads, as expected, were largest at higher elevations 0.4 - 1 water depths above still water level; they were strongest for the near-breaking waves that generated a strong jet at the wall, and decreased somewhat for breaking waves with a weaker jet. Vertical load magnitudes increased strongly with increasing overhang length, and reached an instantaneous maximum of  $F_1^* = 4.6$ in all tests; it is likely that loads would increase further for overhang lengths greater than the maximum  $x_1^* =$ 0.2 tested.

In contrast, horizontal loads on the same blocks showed peak magnitudes that were greatest when the block lower face was 0.1 - 0.5 water depths above the still water level, but decreased strongly for more highly elevated blocks. The horizontal loads increased with increasing wave height over the small range tested, but had minimal sensitivity to the size of overhang.

The concept of time averaged loads is not common in coastal engineering, but the utility of these loads may be shown by comparing the behavior of horizontal and vertical forces. Time-averaged vertical loads decreased extremely rapidly as shown in Figure 14, with largest instantaneous loads over 90% lower when averaged over the time scale  $\Delta t^* = 1$ . Structural failure modes with large mass or response period (e.g. steel moment frames or reinforced concrete systems) may not have sufficient time to respond to the extremely high instantaneous vertical forces, and may instead feel the very much lower long period time averaged loading. However, smaller structural systems (e.g. flooring panels or cladding) may respond on short averaging periods, and will "feel" a different effective load than the larger system. In contrast to vertical forces, time-averaged horizontal loads decreased moderately with increasing averaging period: for an averaging period of  $\Delta t^* = 1$ , horizontal loads decreased by 40-60% from instantaneous maxima. Here, there will be smaller difference in response between larger and smaller scale systems. This necessity of considering structural response characteristics was previously taken into account by Oumeraci et al. (1999), who used either quasi-static or dynamic analyses based on the hydrodynamic loading characteristics for different wave conditions. For all of these, it is becoming clear that the appropriate choice of averaging period (or structural analysis) can not be determined a priori, but is a function of both the structural system under consideration and wave loading characteristics. This entire topic remains an area of active research.

In conclusion, for a block overhanging  $x_1^* = 0.1$ water depths and with a vertical face of  $x_2^* = 0.5$ water depths, results here indicate that:

- Maximum instantaneous vertical loads routinely exceed  $F_1^* = F_1/\rho g h^2 = 1$  for block elevations from  $x_4^* = 1.1 : 2$ , and may exceed  $F_1^* = 2.5$  in extreme cases. For block elevations of  $x_4^* = 2.1 : 2.5$ , a reasonable instantaneous maximum load might be taken as  $F_1/\rho gh^2 = 1$ .
- In contrast, maximum time-averaged vertical loads using  $\Delta t^* = 1$  show little variation with elevations between  $x_4^* = 1.1 : 2.5,$ a maximum of around  $F_1/\rho gh^2 = 0.25$  across most of the range. This represents a very large decrease from the instantaneous loading.
- Maximum instantaneous horizontal loads for block elevations  $x_4^* = 1.1 - 1.3$  may often exceed  $F_2^* = F_2/\rho g h^2 = 1$ , with extreme values seen to  $F_2^* = 1.6$ . Loads decrease strongly at higher elevations, with instantaneous maxima of  $F_2^* = 0.7$  for  $x_4^* = 1.4 : 1.9$ ; and maxima not exceeding  $F_2^* =$ 0.25 for  $x_4^* = 2.0:2.2$ . Horizontal loads at higher block elevations are negligible.
- For averaging periods of  $\Delta t^* = 1$ , horizontal loads show maxima of around  $F_2^* = 0.6$  for  $x_4^* = 1.1 : 1.5$ ;

maxima of  $F_2^* = 0.35$  for  $x_4^* = 1.6 : 1.9$ ; and maxima of  $F_2^* = 0.15$  for  $x_4^* = 2.0:2.2$ .

Overall, the work here demonstrates the utility of numerical techniques in computing wave loads on near-coast structures, and the range of loads that may be generated. Present results show that loads are maximized for waves that are near-breaking, or break directly onto a structure. Instantaneous magnitudes can be very large, but decrease significantly with timeaveraging. Horizontal load estimates are much less sensitive to uncertainties than vertical loads, which depend greatly on details of wave breaking.

#### **Acknowledgments**

The authors would also like to thank the staff in the Center for Research Computing at the University of Notre Dame, who provided great support and computing resources for this work.

#### **Disclosure statement**

No potential conflict of interest was reported by the authors.

#### **Funding**

This work was funded under the National Science Foundation grant CMMI-1435007. The DesignSafe-CI node of the Natural Hazards Engineering Research Infrastructure (NHERI) is acknowledged for the use of their computational facilities.

### References

Altomare, C., J. C. Alejandro, J. M. Crespo, D. Moncho Gmez-Gesteira, T. Suzuki, and T. Verwaest. 2015. "Applicability of Smoothed Particle Hydrodynamics for Estimation of Sea Wave Impact on Coastal Structures." Coastal Engineering 96: 1–12. doi:10.1016/j.coastaleng.2014.11.001.

Attary, N., J. W. van de Lindt, V. U. Unnikrishnan, A. R. Barbosa, and D. T. Cox. 2013. "Methodology for Development of Physics-Based Tsunami Fragilities." Journal of Structural Engineering 143.

Briggs, M., C. Synolakis, G. Harkins, and D. Green. 1995. "Laboratory Experiments of Tsunami Runup on a Circular Island." Pure Applied Geophysics 144 (3-4): 569-593. doi:10.1007/BF00874384.

Cooker, M. J., P. D. Weidman, and D. S. Bale. 1997. "Reflection of a High-Amplitude Solitary Wave at a Vertical Wall." Journal of Fluid Mechanics 342: 141-158. doi:10.1017/S002211209700551X.

Cox, R. A. N., D. B. Zentner, B. J. Kirchner, and M. S. Cook. 2012. "Boulder Ridges on the Aran Islands (Ireland): Recent Movements Caused by Storm Waves, Not Tsunamis." The Journal of Geology 120 (3): 249-272. doi:10.1086/664787.

Cuomo, G., W. Allsop, T. Bruce, and J. Pearson. 2010. "Breaking Wave Loads at Vertical Seawalls and Breakwaters." Coastal Engineering 57 (4): 424–439. doi:10.1016/j.coastaleng.2009.11.005.



- Deshpande, S. S., L. Anumolu, and M. F. Trujillo. 2012. "Evaluating the Performance of the Two-Phase Flow Solver interFoam." Computational Science and Discovery 5 (1): 014016. doi:10.1088/1749-4699/5/1/014016.
- Didier, E., D. R. C. B. Neves, R. Martins, and M. G. Neves. 2014. "Wave Interaction with a Vertical Wall: SPH Numerical and Experimental Modeling." Ocean Engineering 88: 330-341. doi:10.1016/j.oceaneng.2014.06.029.
- Gensis, N. 2013. "PLAN International Aid." Accessed 22 May 2017. https://www.youtube.com/watch?v=KZwGZ\_eX4IU.
- Germain, P. S., I. Nistor, R. Townsend, and T. Shibayama. 2014. "Smoothed-Particle Hydrodynamics Numerical Modeling of Structures Impacted by Tsunami Bores." Journal of Waterway, Port, Coastal, and Ocean Engineering 140 (1): 66-81. doi:10.1061/(ASCE)WW.1943-5460.0000225.
- Goring, D., and F. Raichlen. 1980. "The Generation of Long Waves in the Laboratory." Coastal Engineering 763–783.
- Greenshields, C. J. 2015. "OpenFOAM User Guide (Version 2.4.0)." Accessed https://openfoam.org/.
- Higuera, P., J. Lara, and I. Losada. 2013a. "Simulating Coastal Engineering Processes with OpenFOAM." Coastal Engineering 71: 119-134. doi:10.1016/j.coastaleng.2012.06.002.
- Higuera, P., J. L. Lara, and I. J. Losada. 2013b. "Realistic Wave Generation and Active Wave Absorption for Navier-Stokes Models: Application to OpenFOAM®." Coastal Engineering 71: 102-118. doi:10.1016/j.coastaleng.2012.07.002.
- IHCantabria. 2014. "IHFOAM Manual." Accessed http:// ihfoam.ihcantabria.com/.
- Iturrioz, A., R. Guanche, J. L. Lara, C. Vidal, and I. J. Losada. 2015. "Validation of OpenFOAM for Oscillating Water Column Three-Dimensional Modeling." Ocean Engineering 107: 222-236. doi:10.1016/j.oceaneng.2015.07.051.
- Jacobsen, N. G., D. R. Fuhrman, and J. Fredse. 2012. "A Wave Generation Toolbox for the Open-Source CFD Library: OpenFoam." International Journal for Numerical Methods in Fluids 70 (9): 1073-1088. doi:10.1002/fld.2726.
- Kanoglu, U., and C. Synolakis. 1998. "Long Wave Runup on Piecewise Linear Topographies." Journal of Fluid Mechanics 374: 1-28. doi:10.1017/S0022112098002468.
- Kennedy, A. B., N. Mori, T. Yasuda, T. Shimozono, T. Tomiczek, A. Donahue, T. Shimura, and Y. Imai. 2017. "Extreme Block and Boulder Transport along a Cliffed Coastline (Calicoan Island, Philippines) during Super Typhoon Haiyan." Marine Geology 383: 65–77. doi:10.1016/j.margeo.2016.11.004.
- Kisacik, D., P. Troch, and V. B. Philippe. 2012. "Description of Loading Conditions Due to Violent Wave Impacts on a Vertical Structure with an Overhanging Horizontal Cantilever Slab." Coastal Engineering 60: 201–226. doi:10.1016/j.coastaleng.2011.10.001.
- Kleefsman, K. M. T., G. Fekken, A. E. P. Veldman, B. Iwanowski, and B. Buchner. 2005. "A Volume-of-Fluid Based Simulation Method for Wave Impact Problems." Journal of Computational Physics 206 (1): 363–393. doi:10.1016/j.jcp.2004.12.007.

- Lay, T., H. Kanamori, C. Ammon, M. Nettles, S. Ward, R. Aster, S. Beck et al. 2005. "The Great Sumatra-Andaman Earthquake of 26 December 2004." Science 308 (5725): 1127-1133. doi:10.1126/science.1112250.
- Lugni, C., M. Brocchini, and O. M. Faltinsen. 2006. "Wave Impact Loads: The Role of the Flip-Through." Physics of Fluids 18 (12): 122101. doi:10.1063/1.2399077.
- Mori, N., and T. Takahashi. 2012. "Nationwide Post Event Survey and Analysis of the 2011 Tohoku Earthquake Tsunami." Coastal Engineering Journal 54 (1): 1250001. doi:10.1142/S0578563412500015.
- NOAA. 2013. "National Coastal Population Report, Population Trends from 1970 to 2020." Accessed http:// oceanservice.noaa.gov/facts/coastal-population-report. pdf.
- Oumeraci, H., N. W. H. Allsop, M. B. de Groot, R. S. Crouch, and J. K. Vrijling. 1999. "MAST III/PROVERBS Probabilistic Design Tools for Vertical Breakwaters." Technical Report. Technical University of Braunschweig.
- Paczkowski, K. W., H. R. Riggs, I. N. Robertson, and M. H. Kobayashi. 2014. Reynolds Averaged Navier-Stokes Computational Solution for Experimentally Generated High Velocity Bore Impact on Vertical Walls.
- Peregrine, D. H. 2003. "Water-Wave Impact on Walls." Annual Review of Fluid Mechanics 35 (1): 23-43. doi:10.1146/ annurev.fluid.35.101101.161153.
- Robertson, I. N., K. Paczkowski, H. R. Riggs, and A. Mohamed. 2013. "Experimental Investigation of Tsunami Bore Forces on Vertical Walls." Journal of Offshore Mechanics and Arctic Engineering 135 (2): 021601. doi:10.1115/1.4023149.
- Shafiei, S., B. W. Melville, and A. Y. Shamseldin. 2016. "Experimental Investigation of Tsunami Bore Impact Force and Pressure on a Square Prism." Coastal Engineering 110: 1-16. doi:10.1016/j.coastaleng.2015.12.006.
- Tadepalli, S., and C. Synolakis. 1996. "Model for the Leading Waves of Tsunamis." Physical Review Letters 77 (10): 2141-2144. doi:10.1103/PhysRevLett.77.2141.
- Tomiczek, T., A. Prasetyo, N. Mori, T. Yasuda, and A. Kennedy. 2016. "Effects of a Macro-Roughness Element on Tsunami Wave Amplification, Pressures, and Loads: Physical Model and Comparison to Japanese and US Design Equations." Coastal Engineering Journal 59 (01):
- Tung, C. C., B. Kasal, S. M. Rogers, and S. C. Yeh. 1999. "Behavior of Breakaway Wall Subjected to Wave Forces: Analytical and Experimental Studies." Technical Report. North Carolina Sea Grant.
- Yan, F., C. Zhang, L. Sun, and D. Zhang. 2015. "Experimental Study on Slamming Pressure and Hydroelastic Vibration of a Flat Plate during Water Entry." Journal of Coastal Research 73: 594-599. doi:10.2112/SI1-103.1.
- Yim, S., M. Olsen, K. Cheung, and M. Azadbakht. 2014. "Tsunami Modeling, Fluid Load Simulation, and Validation Using Geospatial Field Data." Journal of Structural Engineering 140: A4014012. doi:10.1061/(ASCE) ST.1943-541X.0000940.